SCIENCE CHINA
Technological Sciences

Special Topic: Impact Dynamics of Structures/Materials
•Article•

https://doi.org/10.1007/s11431-020-1774-1

# Dynamic response of ultralight all-metallic sandwich panel with 3D tube cellular core to shallow-buried explosives

ZHANG DuJiang[1,2,3†], ZHAO ZhenYu[1,2†*], DU ShaoFeng[3], CHEN WeiJie[1,2], YANG Fan[1,2], NI ChangYe[1,2], YANG ZhiKun[3] & LU TianJian[1,2,4*]

[1] *State Key Laboratory of Mechanics and Control of Mechanical Structures, Nanjing University of Aeronautics and Astronautics, Nanjing 210016, China;*
[2] *MIIT Key Laboratory of Multifunctional Lightweight Materials and Structures (MLMS), Nanjing University of Aeronautics and Astronautics, Nanjing 210016, China;*
[3] *State Key Laboratory of Smart Manufacturing for Special Vehicles and Transmission System, Baotou 014030, China;*
[4] *State Key Laboratory for Strength and Vibration of Mechanical Structures, Xi'an Jiaotong University, Xi'an 710049, China*

Received November 3, 2020; accepted January 4, 2021; published online May 13, 2021

The underbody of a vehicle system, either military or civil, is typically made of a relatively thin metallic plate, thus vulnerable to mine blast attacks. To improve the blast resistance, a multitude of protective structures have been proposed as attachments to the thin plate. In the present study, a novel ultralight all-metallic sandwich panel with three-dimensional (3D) tube cellular cores mounted to the vehicle underbody was envisioned as such a protective system. A metallic substrate (mimicking vehicle bottom) was placed above the proposed sandwich panel to construct a sandwich-substrate combinative structure. A series of sandwich panels having 3D tube cellular cores were fabricated via argon protected welding and laser welding. Mechanical responses of the combinative structure subjected to the denotation of 6 kg TNT explosives shallow-buried in dry sand were experimentally measured. Full numerical simulations with the method of finite elements (FE) were subsequently carried out to explore the physical mechanisms underlying the observed dynamic performance and quantify the effects of key geometrical parameters and connection conditions of the protective system. The performance of the proposed sandwich panel under shallow-buried explosives was also compared with competing sandwich constructions having equal mass. Finally, a preliminary optimal design of the 3D tube cellular core was carried out.

**shallow-buried explosive, sand blast test, 3D tube cellular core, sandwich panel, numerical simulation**

**Citation:** Zhang D J, Zhao Z Y, Du S F, et al. Dynamic response of ultralight all-metallic sandwich panel with 3D tube cellular core to shallow-buried explosives. Sci China Tech Sci, 2021, 64, https://doi.org/10.1007/s11431-020-1774-1

## 1 Introduction

Mine blasts and improvised explosive devices (IEDs) have increasingly become dangerous threats to civil/military vehicles and crew life, causing approximately 30% of fatalities during the wars in Afghanistan and Iraq [1–4]. As the typically intensive impulsive load can cause large deformation and severe damage to a vehicle, how to design its main structure (in particular, the underbody) [5] against such blast loading attracts much attention [5–7]. For instance, to reduce the transmitted impulse, vehicles like South African Cassipir, Cougar H, and International MaxxPro all adopted V-shaped hulls, in condition that the total vehicle weight remains unchanged [8–10]. To further reduce the impulse transmission, new concepts such as attaching a sliding plate or a side-vent-channel to the V-shaped plate were proposed [10,11]. However, at present, most existing civil/military vehicles

†These authors contributed equally to this work.
*Corresponding authors (email: sufengxing@foxmail.com; tjlu@nuaa.edu.cn)

have flat floors, accompanied by relatively low gravitational centers, and hence the V-shaped hull design is not appropriate. To address the issue, attaching a lightweight protection structure (e.g., all-metallic sandwich panel with cellular core) to the vehicle underbody has become a feasible strategy [12,13]. Consequently, designing high-performance yet lightweight and relatively thin sandwich constructions that can sustain intensive blast loading becomes a necessity [12,14,15].

According to the type of impulse-transmitting medium considered, there exist underwater blast, air blast, and shallow-buried blast [16]. To attenuate underwater blast loading, fluid-structure interaction (FSI) and high bending resistance of sandwich structures have been exploited [17,18]. However, it has been demonstrated, both analytically and numerically, that the FSI in air is considerably weaker than that in fluid [18,19]. Experimentally, it was revealed that, when subjected to identical air blast loading, all-metallic sandwich panels having metal foam (Figure 1(a)), corrugated (Figure 1(b)) and square honeycomb (Figure 1(c)) cores exhibit superior performance to their monolithic counterpart having identical mass [20–22]. Under air blast, as the FSI has much weakened effect, the high bending resistance of the structure plays a critical role in reducing its displacement [23]. Recently, to further enhance the blast resistance of sandwich structures having prismatic lattice cores (e.g., corrugated plates), filling the interstices of the core with metallic foam (Figure 1(d)) or fluid (Figure 1(e)) was proposed [24–26].

As for blast loading induced by shallow-buried explosives, because the impulse-transmitting medium is much different from either air or water, the physical mechanisms underlying the blast loading that exerts on a protective structure are also considerably different [27]. Specifically, from the initiation of explosion to structural response, three stages in sequel may be classified: (1) impulse transmission between explosives and sand particles, enabling the latter to acquire a high speed; (2) splashing of sand particles; (3) impulse transmission between high-speed sand particles and protective structure, forcing the latter to respond dynamically [7]. Nonetheless, upon explosion, due to the formation of an opaque sand cloud (formed by sand particles and explosion products), the short duration of explosion and the damage/mal-functioning of the measurement instruments as a result of explosion, it is difficult experimentally to characterize in detail the expanding cloud as well as the interaction between the sand particles and the protective structure [12]. Rather, a variety of numerical approaches have been employed to explore the physical mechanisms that underlie the dynamic structural responses observed experimentally. For instance, to investigate the response of a clamped beam subjected to high-speed sand impact, the technique of particle simulation was adopted [28]. At the laboratory scale, in lieu of a sand projectile, impacting with a metallic foam projectile had been envisioned as a feasible experimental technique to simulate blast load caused by shallow-buried explosives [12]. This technique was further improved by substituting the originally uniform foam projectile [12] with a density gradient foam projectile [29]. In fact, tailoring the cellular morphology (density gradient) and launching speed of the foam projectile can generate an impulse of desirable pressure-time morphology [29].

When subjected to high-speed sand impacting, the dynamic behaviors of all-metallic sandwich panels cored with pyramidal trusses [16], hexagonal honeycombs [12], square honeycombs [27] and corrugated plates [23] had been experimentally and numerically investigated, and compared with that of a monolithic plate of equal mass. Because these sandwich constructions exhibit high bending resistance and absorb impact energy via core compression, tension of core members and membrane tension of face sheets [30], the corresponding blast performances in terms of, e.g., rear face displacement, are in general superior to its monolithic counterpart [12,16,23,27]. Among representative sandwich core topologies, square honeycombs and corrugated plates are favored over pyramidal trusses, as the latter have relatively low in-plane tensile properties and are more difficult to fabricate [31]. More recently, a novel cellular structure consisted of three-dimensional (3D) square aluminum tubes

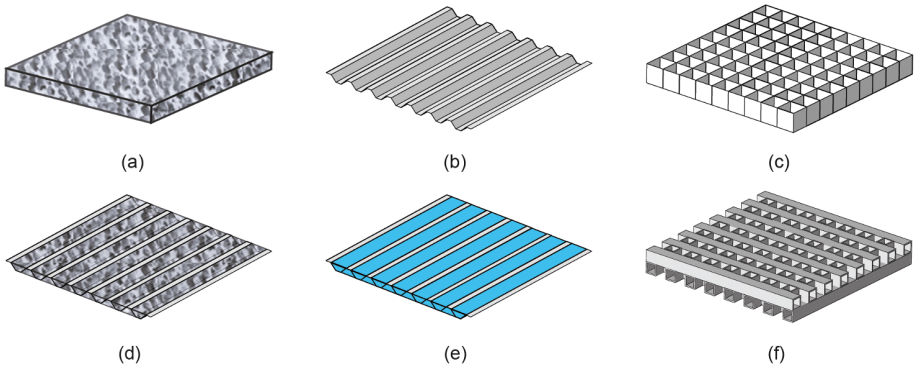


**Figure 1** (Color online) Schematic of representative sandwich core morphologies: (a) cellular metallic foam, (b) corrugated plate, (c) square honeycomb, (d) corrugated plate with inserted metallic foam, (e) corrugated plate filled with fluid, and (f) 3D cellular tubes.

was proposed, as depicted in Figure 1(f), and fabricated via brazing [31]. The performance of the 3D tubular cellular structure was investigated under quasi-static out-of-plane compression, dynamic compression and sand impact [31–33]. It was demonstrated that the tubular cellular structure exhibits a specific energy absorption that increases with its compressive strength and, under sand impact, transmits an impulse 5% lower than its monolithic counterpart of equal mass [31]. At present, there is yet a sandwich structure that employs the 3D tubular cellular structure as its core. It is therefore of interest to further explore the potential of adopting such a structure as the core for sandwich construction against blast loading, thus motivating the current study.

In this study, novel all-metallic sandwich panels cored with 3D cellular tubes (Figure 1(f)) were firstly fabricated with argon protected welding and laser welding. Subsequently, different from most existing studies, to mimic the protection of a vehicle underbody, the fabricated sandwich panel was attached to a monolithic metallic plate (i.e., the bottom supporting plate of the vehicle) to form a sandwich-substrate combinative system. Dynamic performance of the sandwich-substrate combination subjected to the denotation of explosives (6 kg TNT) shallow-buried in dry sand was then measured, consistent with the 2b protection level of the NATO AEP-55 standard. Full numerical model was also established with the method of finite elements (FE) to explore the physical mechanisms underlying the observed dynamic responses, validated against experimental measurements. Finally, the performance of the proposed sandwich panel was compared with competing sandwich constructions having equal mass, and a preliminary optimal design of the 3D tube cellular core was carried out.

## 2 Sandwich panel with 3D tube cellular core: Morphology and fabrication

### 2.1 Morphology

Figure 2 depicted schematically the morphological details of the proposed sandwich panel with 3D tube cellular core. The core was consisted of three mutually perpendicular arrays of square tubes, i.e., the *x*-tubes, the *y*-tubes and the *z*-tubes, oriented separately along the *x*, *y* and *z* directions. The tubes had identical width $l_t$ and wall thickness $t_t$, although this scenario would change when the tubes were optimally designed using the FE method (Sect. 5.4). The distance between neighboring *x*-tubes as well as that between neighboring *y*-tubes was equal to the tube width (i.e., $l_t$). The *x*-tubes were connected to the front plate (facing the blast impact), the *y*-tubes were placed above the *x*-tubes and connected to the rear plate, while the *z*-tubes were inserted between the *x*- and *y*-tubes (Figure 2). Relevant geometric

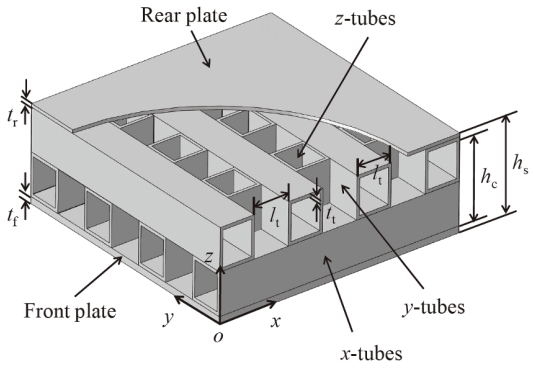


**Figure 2** Schematic of sandwich panel with 3D tube cellular core.

and physical parameters were: sandwich height $h_s$, front plate thickness $t_f$, 3D tube cellular core height $h_c$, rear plate thickness $t_r$, front plate density $\rho_f$, tube density $\rho_t$, and rear plate density $\rho_r$. The relative density of the 3D tube cellular core could thence be expressed as [32]

$$\overline{\rho}_t = \frac{3(l_t - t_t)t_t}{l_t^2}. \quad (1)$$

The mass per unit area of the sandwich panel, $\overline{M}$, was

$$\overline{M} = \rho_f t_f + \overline{\rho}_t \rho_t h_c + \rho_r t_r. \quad (2)$$

In Supporting Information, the overall stiffness of the sandwich panel with 3D tube cellular core subjected to out-of-plane uniform pressure was characterized analytically and numerically.

### 2.2 Fabrication

Figure 3 illustrated schematically the procedures for fabricating the proposed sandwich panel with 3D tube cellular core, based on a combined assembling method of argon protected welding and laser welding. More details were summarized as follows.

(1) With reference to Figure 3(a), upon placing identical square *x*-tubes periodically on the front plate, the two were connected using argon protected welding, and the distance between adjacent *x*-tubes was the same as the tube width. The distance between two neighboring welding seams was 50 mm, with each seam having a width of ~15 mm, as shown in Figure 4(a).

(2) As shown in Figure 3(b), upon placing identical *y*-tubes periodically on top of the *x*-tubes, the two groups of tubes were connected via argon protected welding, thus forming an orthogonal tube array. Figure 4(b) displayed typical welding seams between the *x*- and *y*-tubes.

(3) As shown in Figure 3(c), the *z*-tubes were inserted (with the help of a hammer) into the interstices of the orthogonal *x*- and *y*-tube array and then welded to the *y*-tubes. Figure 4(b) also displayed typical welding seams between the *y*- and *z*-tubes.

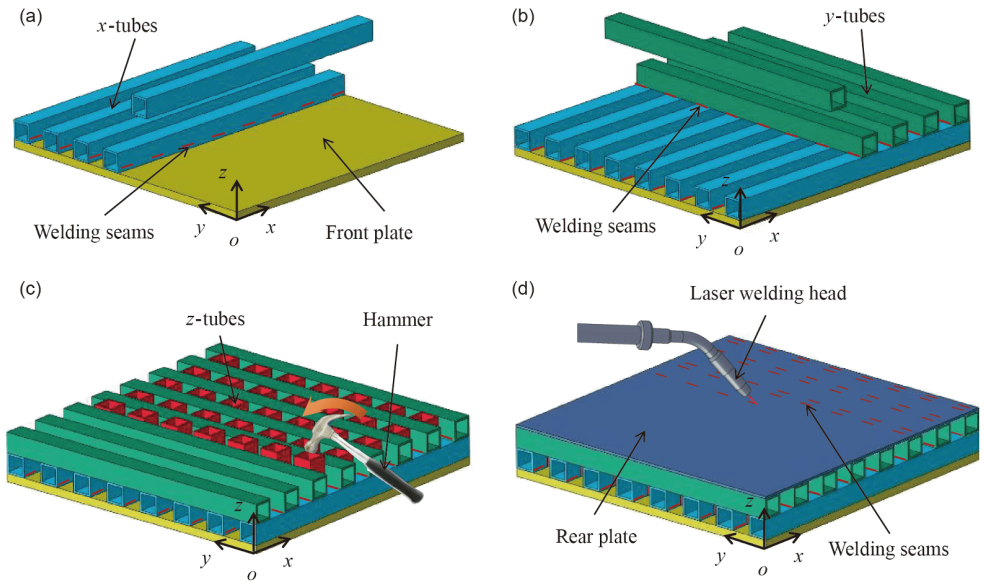


**Figure 3** (Color online) Fabrication procedures of sandwich panel with 3D tube cellular core. (a) Welding *x*-tubes to front plate; (b) welding *y*-tubes to *x*-tubes; (c) inserting *z*-tubes; (d) welding between rear plate and *y*-tubes.

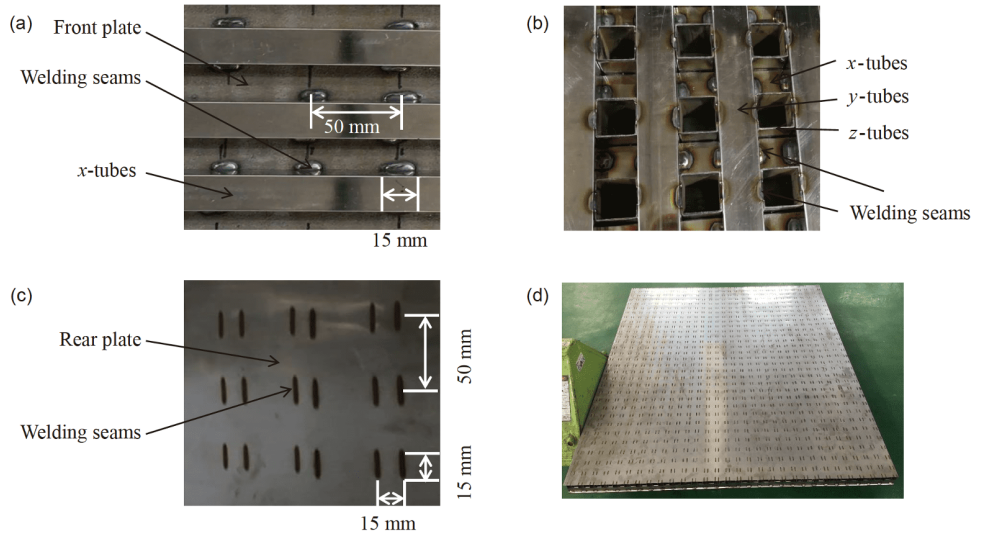


**Figure 4** (Color online) Photographs of (a) argon protected welding between *x*-tubes and front plate, (b) argon protected welding between *x*- and *y*-tubes, (c) laser welding between *y*-tubes and rear plate, and (d) as-fabricated sandwich panel.

(4) The rear plate was placed on top of the *y*-tubes and the two were connected with laser welding, as shown schematically in Figure 3(d). Each *y*-tube was connected to the rear plate with two welding seams 15 mm apart, and the width of each seam was ~15 mm. Within one array of the welding seams, the distance between two neighboring seams was fixed at 50 mm, as shown in Figure 4(c).

Figure 4(d) presented a typical as-fabricated sandwich panel. The front plate was made of Weldox 960, while both the tube cellular core and the rear plate were made of 304 stainless steel. For the present blast tests with shallow-buried explosives, two sandwich panels were fabricated, with detailed geometric parameters summarized in Table 1. One sandwich panel had a front plate thickness of 10 mm, while the other had 8 mm. Correspondingly, the former had a mass per unit area of 131.2 kg $m^{-2}$ and the latter had 115.5 kg $m^{-2}$.

## 3 Blast test with shallow-buried explosives

### 3.1 Model of blast test

With reference to Figure 5, to mimic the protection of a vehicle underbody against the detonation of explosives buried under shallow sand, the proposed sandwich panel

**Table 1** Geometric parameters of as-fabricated sandwich panels with 3D tube cellular cores

| Sandwich panel | $l$ (mm) | $h_s$ (mm) | $\overline{M}$(kg m$^{-2}$) | $t_f$ (mm) | $l_t$ (mm) | $t_t$ (mm) | $\overline{\rho}_t$ | $t_r$ (mm) |
|---|---|---|---|---|---|---|---|---|
| 1 | 1500 | 61 | 131.2 | 10 | 25 | 1 | 0.115 | 1 |
| 2 | 1500 | 59 | 115.5 | 8 | 25 | 1 | 0.115 | 1 |

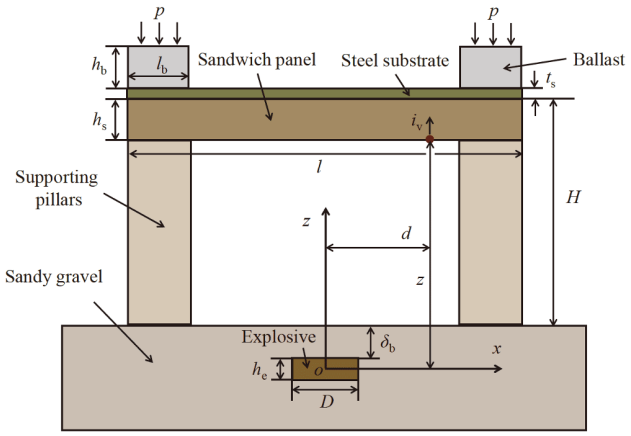


**Figure 5** (Color online) Schematic of sandwich-substrate combinative structure subjected to shallow-buried explosive. A 3D view of the setup was presented in Figure 6(a).

with 3D tube cellular core was placed underneath a monolithic plate (i.e., the substrate as termed in the current study) of thickness $t_s$, with the plate positioned at a distance $H$ above the ground. For simplicity, the sandwich panel and the substrate were assumed to be square in shape, with identical side length $l$. The sandwich panel had a total height of $h_s$. On top of the substrate, a square box of length $l$, width $l_b$ and height $h_b$ was placed, which was subjected to a pressure $p$ that mimicked the weight of the vehicle (see also the 3D view shown in Figure 6(a)). Beneath the sandwich panel, at its four corners, supporting pillars were placed to support the weight of the sandwich-substrate combination as well as the additional weight mimicking that of the vehicle (Figure 6).

Beneath the center of the sandwich-substrate combination, cylindrical TNT explosive with mass $m_e$ , diameter $D$, height $h_e$ and explosive energy release $E_e$ was buried under sandy gravel of height $\delta_b$ and density $\rho_s$. Let $z$ and $d$ denote separately the vertical and lateral distance between the explosive and the impulse integration point on the front face of the sandwich (Figure 5). Upon detonation of the shallow-buried TNT explosive, let $i_v$ denote the impulse transmitted to the sandwich panel per unit area. While the exact value of $i_v$ is somewhat difficult to calculate, to a good approximation it had been determined in an empirical manner. For the setup shown in Figure 5, $i_v$ could be expressed as [34]

$$i_v(x,y) = 0.1352\left(1+\frac{7}{9}\frac{\delta_c}{z}\right)\left(\frac{\tanh(0.9589\xi d)}{\xi d}\right)^{3.25}\sqrt{\frac{\rho_s E_e}{z}}, \quad (3)$$

where

$$\delta_c = \delta_b + \frac{h_e}{2}, \quad (4)$$

$$\xi = \frac{\delta_c}{z^{5/4}S^{3/8}\tanh\left(\left[2.2\frac{\delta_c}{z}\right]^{3/2}\right)}, \quad (5)$$

$$S = \frac{\pi D^2}{4}. \quad (6)$$

In eq. (3), $d$ is the lateral distance between the explosive and the impulse integration point on the front face of the sandwich (Figure 5). Thus, with $d = \sqrt{x^2+y^2}$ , the impulse $i_v$ was non-uniformly distributed on the front face.

Note that the properties of sandy gravel (e.g., grain size, grain hardness, mass density, water content, etc.) affect the effective transmission of impulse. Clarke et al. [35] systematically investigated how grain size, density, water content and the like affect impulse transfer by comparing the performances of explosive shallow buried under 5 different types of sandy gravel. They found insignificant influence of grain size, but identified the key roles played by sand density and water content. In a previous study [36], we investigated, both experimentally and numerically, the effects of sand filling on the dynamic response of corrugated core sandwich beams. In our FE model, the sand was modeled using a group of 3D rigid spherical particles. FE simulations of the sand compression test were conducted by compressing the discrete particles via a rigid punch. As an important factor in discrete particle modeling was the correct determination of contact properties between particles, we used both the slump test and constrained compression test were used to calibrate the contact parameters [36]. The slump test aimed to estimating the friction between particles while the purposed of the constrained compression test was to estimate the contact stiffness. With sand grains regarded as rigid particles, the numerically simulated nominal strain versus nominal stress responses agreed well with experimental measurements [36]. The calibrated contact parameters of sand particles were employed to simulate the permanent mid-span deflection and deformation modes of sand-filled sandwich beams subjected to shock loading; the numerical simulation results agreed well with those observed experimentally. Therefore, in the current study, we also assumed the sand particles were rigid.

In eq. (3), the influence of sand density (i.e., mass density $\rho_s$ of sand particles) was accounted for, but not that of water content. Before each explosion was carried out, we measured the sand density but not water content, because we assumed the latter was negligible due to the relatively dryness of the

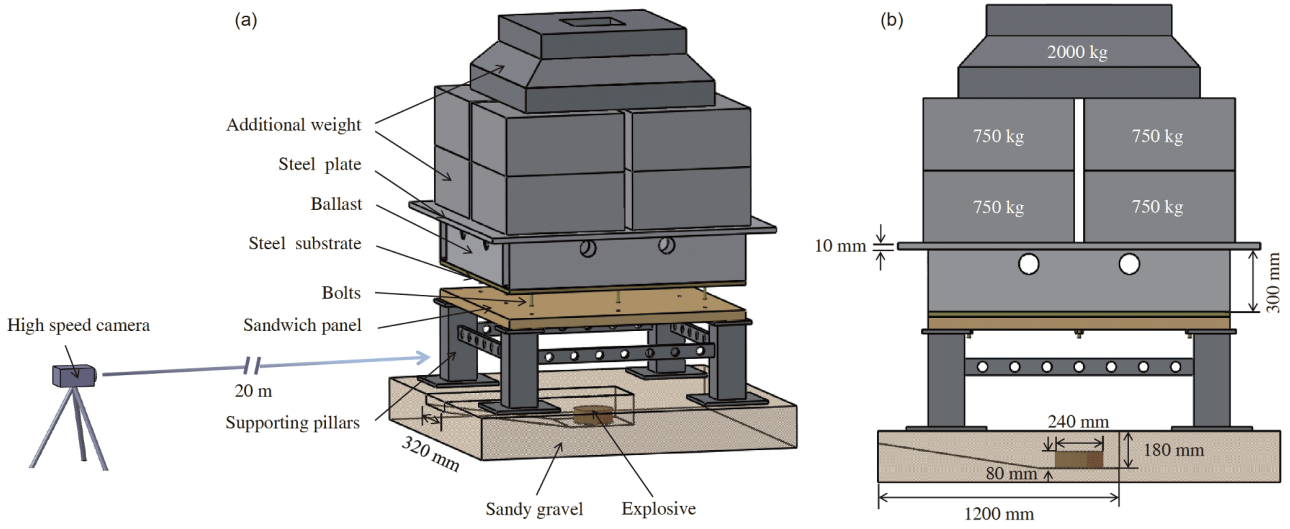


**Figure 6** (Color online) Schematic diagram of experimental setup for blast testing with shallow-buried explosive. (a) Three-dimensional diagram; (b) two-dimensional diagram.

sandy gravel used on site. As the focus of the current study was placed upon evaluating the dynamic performance of the sandwich-substrate combination when subjected to shallow-buried explosives, we selected a conventional sandy gravel and ignored the influence of grain size, hardness and water content.

### 3.2 Experimental setup

In accordance with the blast model of Figure 5, Figure 6 depicted the experimental setup for investigating the dynamic performance of the as-fabricated sandwich panel under shallow-buried explosive. The setup was mainly consisted of four supporting pillars, a sandwich protection structure, a steel substrate, a ballast, a steel plate and an additional weight. To record the whole process of explosion, a high-speed camera (FASTCAM Mini Ax200: 8000 frames per second and exposure time 1 μs) was placed 20 m away from the setup.

To mimic the weight of a protected vehicle, the additional weight was set at 8 tons (i.e., $M_a$=8 t), which consisted of several pre-designated concrete blocks. Upon detonation, in order for the sandwich-substrate combination to have sufficient room for deformation and also for preventing the additional weight (concrete blocks) to exert a follow-up impact on the combination, which may cause further deformation and hence affect the final experimental result, a square-shaped ballast made of Q345B steel was placed in between the combination and the additional weight (Figure 6). The ballast had side length $l$=1500 mm, width $l_b$=150 mm and height $h_b$=300 mm, thus was hollow in its center. A supporting plate was placed directly above the ballast and the two were not connected via welding or bolting. The supporting plate, which was made of Weldox 960 steel and square in shape, had side length $l_{sp}$=1800 mm and thickness $t_{sp}$=10 mm. Similarly, the ballast and the steel substrate were in direct contact but not connected, either via welding or bolting. The test specimen (i.e., the sandwich-substrate combination) was placed immediately above the four supporting pillars. The sandwich panel and the steel substrate were connected via bolts, while the supporting pillars was in direct contact with the sandwich panel but not connected with it via bolts, as shown in Figure 6.

In accordance with the 2b protection level of the NATO AEP-55 standard, cylindrical TNT explosive ($m_e$=6 kg, $D$=240 mm and $h_e$=80 mm) was buried under sandy gravel of height $\delta_b$=100 mm, directly beneath the center of the sandwich-substrate combination. The sandy gravel groove housing the explosive was 1200 mm×320 mm×180 mm in dimensions, as shown in Figure 6. The sandy gravel used in the present study had a density of $\rho_s$=1673 kg m$^{-3}$ and a grading curve as shown in Figure 7.

### 3.3 The blast process

With the experimental setup of Figure 6, Figure 8 displayed the sequential processes of sand expansion when subjected to the detonation of 6 kg shallow-buried TNT explosive. A high-speed camera was used to record the blast processes with 8000 frames per second, starting at $t$=0 ms. Upon detonation, sand was ejected out from the sand-filled groove at $t$=8 ms, which then interacted with the front face of the sandwich panel at $t$=12 ms (Figure 8(b)–(d)). Subsequently, increasingly more sand was ejected, forming an expanding cloud of sand particles and explosion products. After the detonation was complete, the final deformation morphology of each sandwich panel was measured, with the corresponding residual deformation of steel substrate. Both were

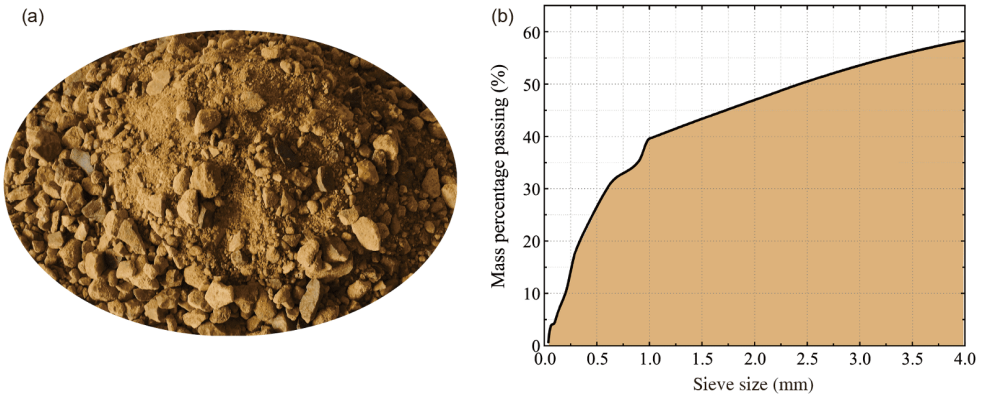


**Figure 7** (Color online) Sandy gravel for shallow-buried explosive: (a) photograph and (b) grain size distribution.

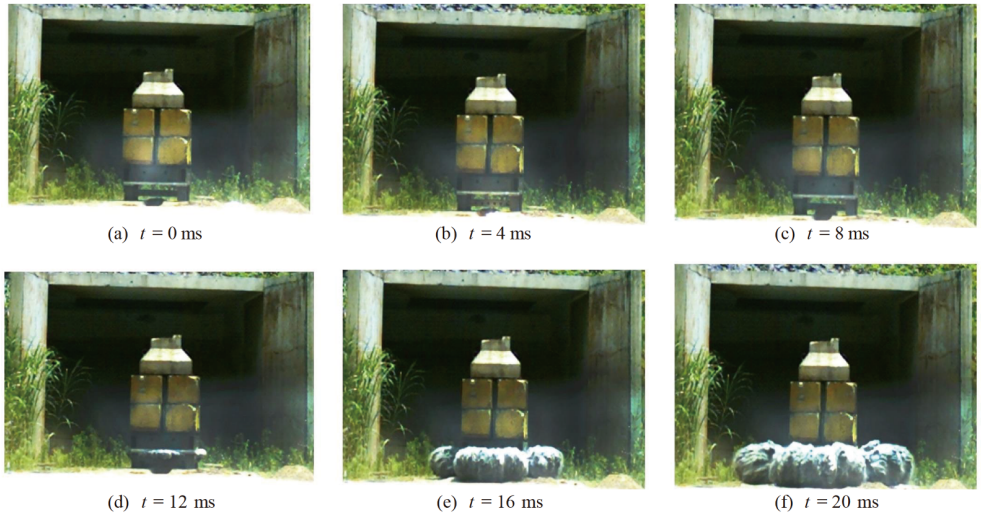


**Figure 8** (Color online) Sequential expanding processes of sand subjected to detonation of shallow-buried explosive.

compared with those calculated from full numerical simulations, as detailed in the next section.

## 4 Numerical simulation

### 4.1 Finite element model

Commercially available FE code ABAQUS was utilized to numerically simulate the blast process. Due to symmetry, only a quarter of experimental setup was simulated, as shown schematically in Figure 9; for simplification, the additional weight, steel plate and ballast placed on top of the test specimen (mimicking the weight of a vehicle), as shown in Figures 6 and 8, were simplified as a square steel frame of identical weight. The steel substrate, the front plate and the square frame were all meshed using linear hexahedral elements of type C3D8R, while the rear plate and the 3D tube cellular cores were meshed using shell elements of type S4R. In the simulation, the bolts in the boundary area were not considered. The $x$-tubes were connected to the front plate and the $y$-tubes using the "Tie" constraint in ABAQUS. The $y$-tubes were connected in the same way to the rear plate. At each junction of the $y$-tube, the $z$-tube and the rear plate, "Tie" constraint was applied to the $y$- and $z$-tubes in order to mimic the factual welding connection there. Otherwise, the $x$- and $z$-tubes as well as the $y$- and $z$-tubes were in direct contact (recall that, during fabrication, the $z$-tubes were inserted with the help of a hammer) but not welded together. General contact was applied on relevant interfaces in the current model.

To obtain optimal mesh sizes for FE simulations, a mesh convergence study was carried out. Eventually, for balanced computational cost and numerical accuracy, the following mesh sizes were selected: 10 mm for front plate, rear plate, and steel substrate, 5 mm for 3D tube cellular core, and 30 mm for square frame, as displayed in Figure 9.

A blast pulse period was typically on the order of a tenth of a millisecond [20], while the response time for a structure with a width of one meter or more was several milliseconds. Therefore, the pressure pulse acting on the structure could be

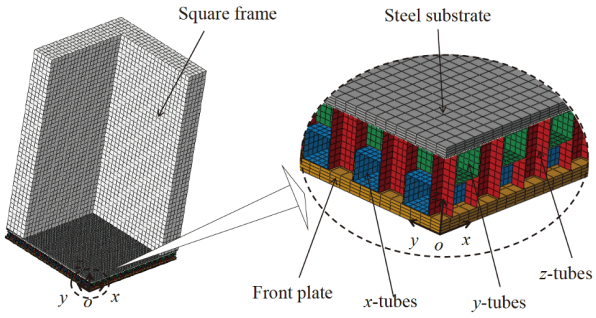


**Figure 9** (Color online) Finite element model.

replaced by the initial pulse, for the response time of the structure was much larger than the period of the blast pulse [37]. In the current study, as the blast impulse on the structure varied with the $x$, $y$, and $z$ coordinates according to eq. (3), a nonuniform initial velocity [20] was applied as the initial condition on the front plate of the sandwich panel. The initial velocity was $v(x,y) = i_v(x,y)/\rho_f t_f$ with $\rho_f$ and $t_f$ being the density and thickness of the front plate, respectively.

### 4.2 Constitutive models

Both the substrate and the front plate of the sandwich panel were made of Weldox 960. As Weldox 960 and Weldox 900 had similar chemical compositions [6,38], the material parameters of the latter were used for constitutive modeling. Both the rear plate and the 3D tube cellular core were made of 304 stainless steel, which was modeled using the Johnson-Cook constitutive model [6,39]. According to this model, the flow stress was given by

$$\sigma = \left[A + B\left(\varepsilon_e^{pl}\right)^n\right]\left[1 + C\ln\left(\frac{\dot{\varepsilon}_e^{pl}}{\dot{\varepsilon}_0}\right)\right](1-\theta^m), \tag{7}$$

where $\dot{\varepsilon}_0$ is a reference strain rate, $\varepsilon_e^{pl}$ is the equivalent plastic strain, $\dot{\varepsilon}_e^{pl}$ is the equivalent plastic strain rate, and $A$, $B$, $C$, $n$, and $m$ are experimentally derived material constants. Further, $\theta$ is a normalized temperature, defined as

$$\theta = \frac{T - T_{tr}}{T_M - T_{tr}}, \tag{8}$$

where $T$ is the absolute temperature, $T_M$ is the melting temperature, and $T_{tr}$ is the transition temperature.

Material parameters used in the current FE simulations were listed in Table 2. As no cracks were found in either the sandwich structure or the steel substrate, material failure (fracture) was not considered.

### 4.3 Validation against experimental results

To reveal the final deformed morphology of each sandwich specimen after explosion, a quarter of the specimen was cut off and compared with that obtained via FE simulation, as shown in Figure 10. The FE simulation results showed that outward bulging occurred in all parts of the specimen and the 3D tube cellular core was significantly compressed, especially in the central area, consistent with the experimental results, as shown in Figure 10(a) and (b). While the extent to which a tube was compressed gradually decreased as it was located further away from the center, shear deformation failure occurred in tubes placed close to the boundary adjacent to the heavy steel frame, which was particularly acute during experiment. Correspondingly, obvious plastic hinges were formed on the substrate plate near its boundary region, immediately above the shear deforming region of the tube core: again, the FE simulations agreed well with the experimental results, as shown in Figure 10(c).

For the two sandwich specimens of Table 1, the numerically calculated residual deformation $\delta$ of the substrate was compared with that measured in Table 3. The residual deformation was defined here as the displacement of the midpoint of the substrate in the $z$-direction relative to the displacement of its corner point (the vertex), as illustrated in Figure 10. Good agreement was achieved, with relative errors less than 10%. Given the complexity involved in the proposed sandwich panel with 3D tube cellular core (Figure 3) and the experimental setup with shallow-buried explosives (Figure 8), the accuracy of the present FE model was considered reasonable. Subsequently, systematic simulations were carried out with the FE model to better understand the physical mechanisms underlying the dynamic responses of the proposed sandwich structure and quantify

**Table 2** Material constants used for constitutive modeling [6,39]

| Material | Notations | 304 stainless steel | Weldox 900 |
|---|---|---|---|
| Young's modulus | $E$ (GPa) | 193 | 210 |
| Poisson ratio | $v$ | 0.3 | 0.33 |
| Density | $\rho$ (kg m$^{-3}$) | 7800 | 7850 |
| Yield stress constant | $A$ (MPa) | 310 | 992 |
| Strain hardening constant | $B$ (MPa) | 1000 | 364 |
| Strain hardening exponent | $n$ | 0.65 | 0.568 |
| Strain rate hardening | $C$ | 0.034 | 0.0087 |
| Temperature softening | $m$ | 1.05 | 1.131 |
| Reference strain rate | $\dot{\varepsilon}_0$ (s$^{-1}$) | 0.001 | 0.0005 |
| Transition temperature | $T_{tr}$ (K) | 293 | 293 |
| Melting temperature | $T_M$ (K) | 1800 | 1800 |
| Specific heat | $C_p$ (J/(kg K)) | 450 | 452 |

**Table 3** Residual deformation ($\delta$) of the steel substrate

| Specimen | $h_s$ (mm) | $\overline{M}$ (kg m$^{-2}$) | Measured $\delta$ (mm) | Calculated $\delta$ (mm) | Relative error |
|---|---|---|---|---|---|
| 1 | 61 | 131.2 | 74 | 81 | 9.46% |
| 2 | 59 | 115.5 | 88 | 96 | 9.09% |

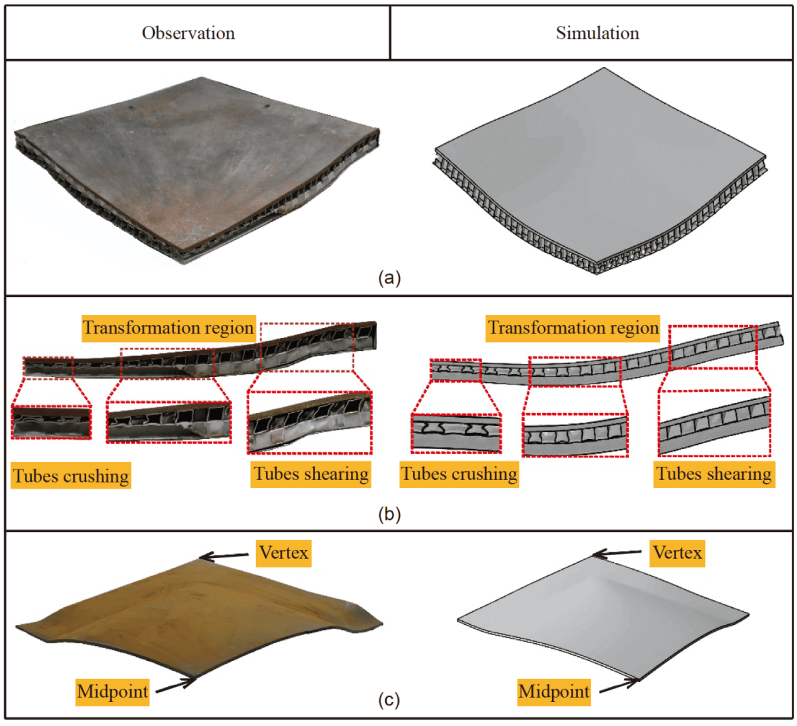


**Figure 10** (Color online) Comparison between experimentally observed specimen after detonation and FE simulation result: (a) viewpoint from front plate, (b) cross-sectional view, and (c) deformed steel substrate.

the influences of key geometrical and processing parameters on its blast resistance.

## 5 Results and discussion

### 5.1 Failure modes and plastic dissipation energy

As shown in Figure 8, from high speed photography, it was difficult to capture in detail the dynamic response of the sandwich after shallow-buried explosive was detonated. The validated FE simulation approach was therefore employed to characterize the response process, the failure modes, and the plastic dissipation energy by each constituent.

Upon detonation, the numerically predicted non-dimensional midpoint displacements of the front plate, the rear plate and the substrate were plotted as functions of time in Figure 11, with corresponding snapshots showing deformation evolution of the structure displayed in Figure 12. For the plotting, the sandwich panel had a surface mass density of $\overline{M}$ = 131.2 kg m$^{-2}$. Midpoint displacements of the substrate, the rear plate and the front plate all increased sharply after detonation was initiated, reaching a peak and then gradually decreased. Due to compression of the tube cellular core as shown in Figure 12(b), the front plate exhibited a larger midpoint displacement than that of the rear plate. Before $t$= 0.4 ms, the rear plate and the substrate moved at the same speed while, at $t$=1.2 ms, the latter had a considerably larger midpoint displacement than the former, implying that separation between the two occurred as shown in Figure 12(d). Subsequently, the central portions of the sandwich and the substrate continued to move upward while those in the boundary region moved somewhat downward, with the sandwich-substrate separation line moving correspondingly toward the boundary. At $t$=2.1 ms, the substrate and the rear plate again had the same midpoint displacement, as shown in Figure 12(e). The results of Figure 12(f) suggested that, beyond $t$=2.1 ms, the sandwich and the substrate were separated again in the central region. Note also that the nu-

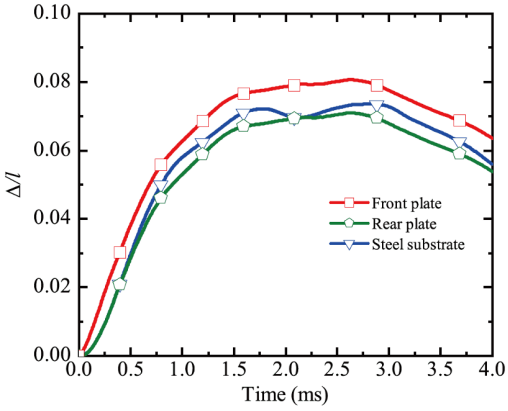


**Figure 11** (Color online) Numerically calculated midpoint displacements of the rear and front plates of sandwich panel as well as the substrate protected by sandwich panel, plotted as functions of time after detonation of shallow-buried explosive. The sandwich panel had a surface mass density of $\overline{M}$ = 131.2 kg m$^{-2}$.

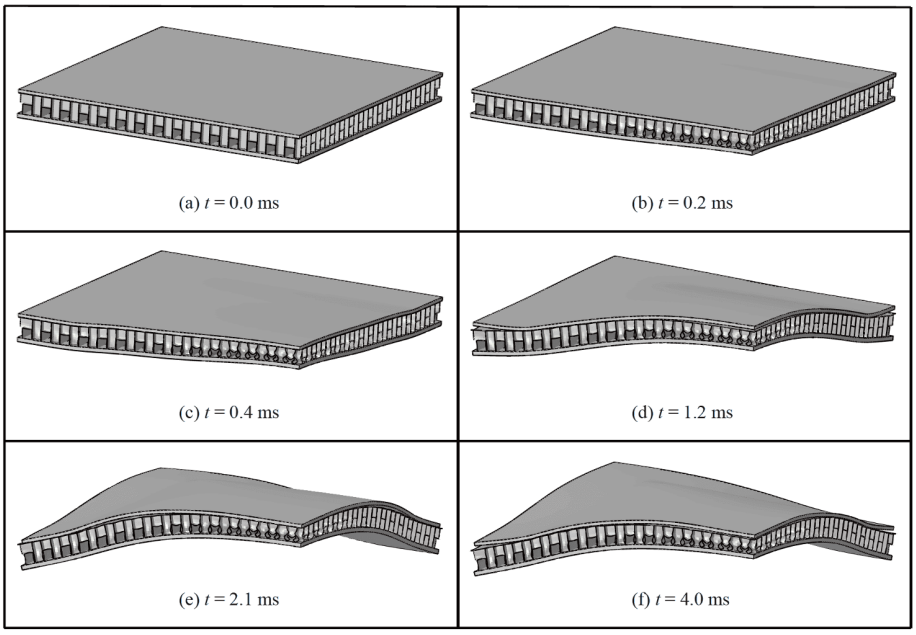


**Figure 12** ABAQUS screenshots showing deformation evolution of sandwich-substrate combinatory structure subjected to sand blast, with a quarter of the structure displayed.

merically simulated deformation modes of both the sandwich and the substrate, i.e., Figure 12(f), were in close agreement with those experimentally observed in Figure 10.

After characterizing the dynamic responses of the combinative structure, its plastic energy dissipation was analyzed. For each substructure, Figure 13(a) plotted its plastic dissipation energy as a function of time; the evolution of total plastic dissipation energy of the sandwich-substrate system was also presented in Figure 13(a). To better understand the energy absorbing capacity of the proposed sandwich panel, corresponding energy absorption curves for the 3D cellular tubes as well as the *x*-, *y*- and *z*-tubes were displayed in Figure 13(b).

It could be seen from Figure 13(a) that the total plastic dissipation energy of the sandwich-substrate combination initially increased and then tended to flatten with the increase of time. According to the failure modes and characteristics of energy absorption of the sandwich-substrate combination, its dynamic response may be divided into three stages.

(1) During the first stage (0–0.4 ms), the *x*-, *y*- and *z*-tubes placed in the central portion of the sandwich experienced intense compressive deformation, as shown in Figure 12(a)–(c), and crushing of the 3D tube cellular core was the main failure mode. Correspondingly, the core dissipated most of the energy during this stage, accounting for nearly 100% of the total absorption. Among the *x*-, *y*- and *z*-tubes, the *z*-tubes absorbed more energy, followed in order by the *x*- and *y*-tubes, with the *z*-tubes absorbing 100% more than that absorbed by the *x*- and *y*-tubes together (Figures 13(b) and 14(b)).

(2) During the second stage (0.4–2.1 ms), in-plane tensile plastic deformation occurred in the front face, in the back face and in the substrate plate, as shown in Figure 15, enabling the sandwich-substrate combination to continue absorbing appreciable energy (Figures 13 and 14). At $t$=0.4 ms, the central portions of both the front and back faces entered the plastic regime and, due to the constraint of the ballast on deformation of the steel substrate at its edges, both the back face and the substrate also entered plastic regime in this region, with the boundary of plastic regime expanding towards their central portions. At $t$=1.2 ms, plastic deformation in the boundary portion of the front face and the central portion of the substrate became new source of energy absorption. As shown in Figure 14(a), in stage 2, as the (plastic) energy absorbed by the front face, the back face and the substrate gradually increased (Figure 13(a)), the percentage of total energy absorbed by the 3D cellular tube core sharply decreased, from approximately 100% to about only 55%.

(3) During the third stage (beyond $t$=2.1 ms), while the core stopped absorbing energy, there was only slight increase of energy absorbed by the front/back faces and the substrate; Figures 13 and 14. Eventually, the sandwich-substrate combination exhibited a distinctive deformation mode as shown in Figure 12(f), consistent with that observed experimentally.

Figure 16 compared the percentage of plastic energy absorbed by each substructure at $t$=4 ms, i.e., towards the end of explosion wherein the combinatory structure almost stopped absorbing new energy. With 28.4%, the *z*-tubes absorbed more energy than the others, followed in sequel by the front face (20.8%), the substrate (16.0%), the *x*-tubes (13.1%), the back face (11.4%), and the least absorbing

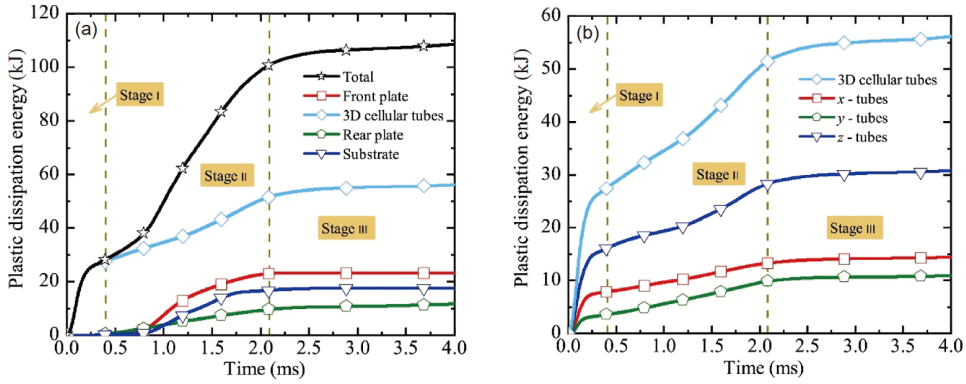


**Figure 13** (Color online) Plastic dissipation energy versus time curve for (a) each substructure as well as the sandwich-substrate system, and (b) the 3D cellular tubes as well as the *x*-, *y*- and *z*-tubes in sandwich-substrate combination.

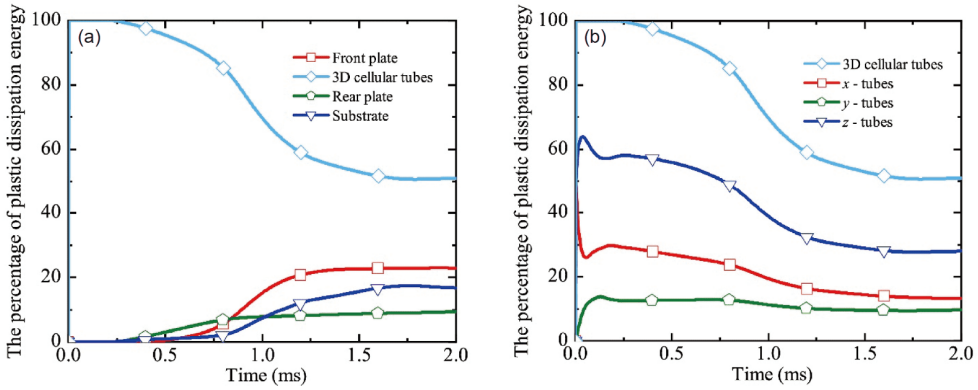


**Figure 14** (Color online) Percentage of plastic dissipation energy plotted as a function of time for (a) each substructure, and (b) the 3D cellular tubes as well as the *x*-, *y*- and *z*-tubes in sandwich-substrate combination.

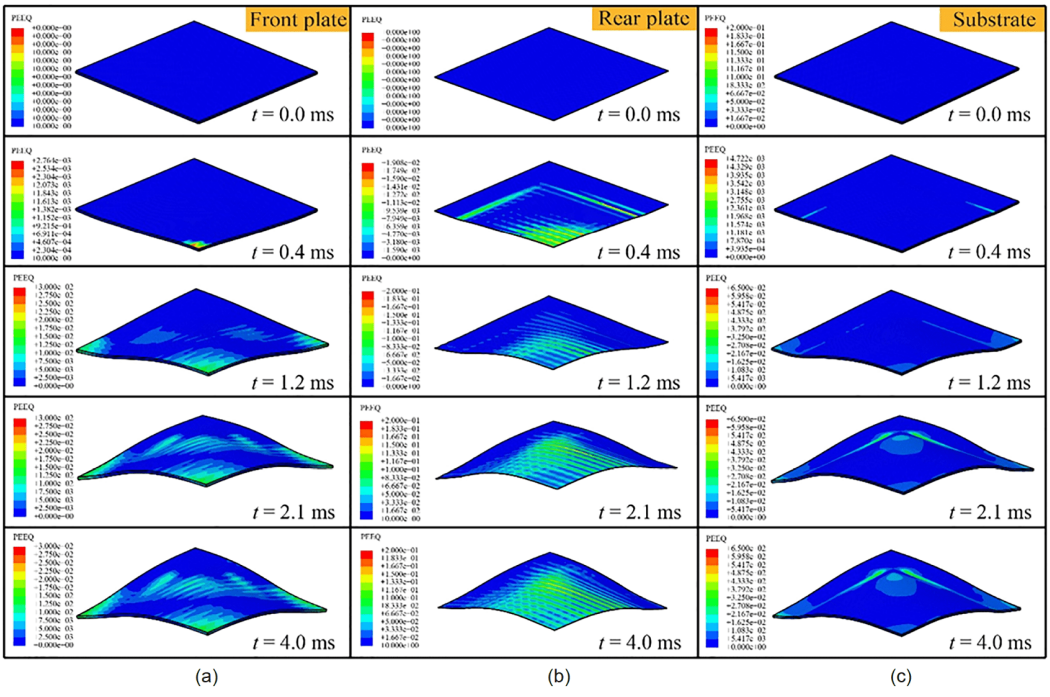


**Figure 15** (Color online) Evolution of equivalent plastic strain diagram for (a) front face, (b) rear face, and (c) steel substrate.

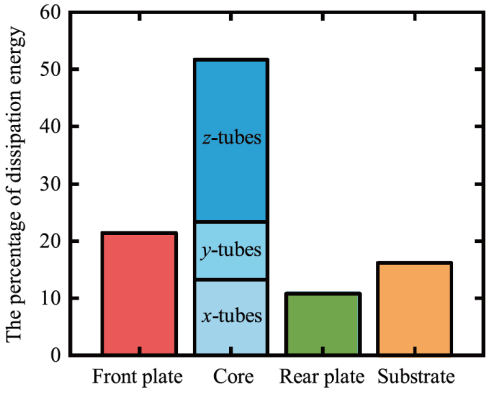


**Figure 16** (Color online) Percentage of energy dissipated by each substructure in sandwich-substrate combination at $t$=4 ms.

$y$-tubes (10.2%). From Figure 16, it could be further seen that the 3D tube cellular core was the main energy absorber, accounting for more than 50% of total plastic energy dissipation, whereas the front face was more effective in energy absorption than the back face and the substrate.

Figure 17 presented the energy absorbed by each type of tube per unit mass placed at different locations of the core. The position of an $x$-tube varies along the $y$-axis, the position of a $y$-tube varies along the $x$-axis, and the position of a $z$-tube varies along both the $x$-axis and the $y$-axis, as illustrated in Figure 9. According to eq. (3), the central portion of the front face acquired most of the incoming blast impulse. Correspondingly, the tubes placed in the central regime were more severely compressed and hence absorbed more energy relative to those placed near the boundary regime. In particular, the $z$-tubes absorbed considerably more energy than the $x$- and $y$-tubes, consistent with the results of Figures 13 and 14.

## 5.2 Parameter study

### *5.2.1 The gap between substrate and sandwich panel*

Most existing civil/military vehicles are not properly designed against intensive blast loading and hence need to install lightweight protection structures for enhanced survival capability. However, as the bottom of a vehicle is often not a perfectly flat structure, upon installing such a protection structure, a gap inevitably exists between the bottom plate and the protection structure. It is therefore of importance to investigate how such a gap may affect the performance of the protection structure.

As illustrated in Figure 18, let a gap of thickness $d_{sr}$ exists between the sandwich and the substrate it aims to protect. Figure 19 plotted the normalized residual deformation, $\delta/l$, of the substrate as a function of normalized impulse, $I/[M(\sigma_0/\rho_f)^{1/2}]$, for selected values of $d_{sr}/t_f$ where $I$ was the impulse per unit area and $\sigma_0$ was the yield stress of the front face. With the normalized impulse fixed at

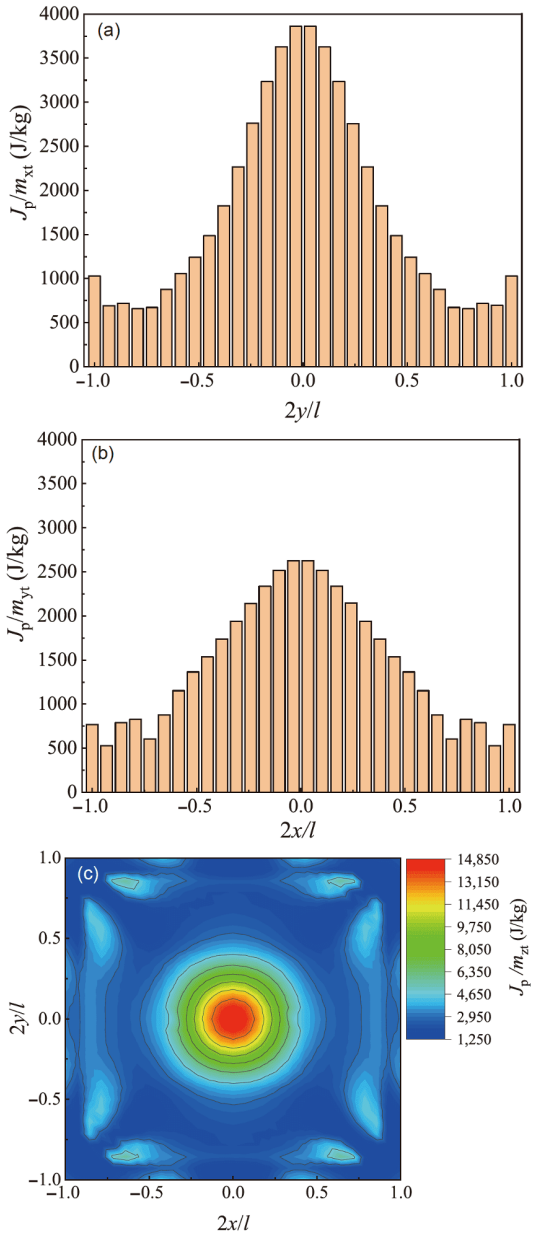


**Figure 17** (Color online) Plastic energy absorbed by each tube per unit mass: (a) $x$-tubes, (b) $y$-tubes and (c) $z$-tubes. $x$ and $y$: tube coordinates; $J_p$: plastic dissipation energy of each tube; $m_{xt}$: mass of $x$-tube; $m_{yt}$: mass of $y$-tube; $m_{zt}$: mass of $z$-tube.

$I/[M(\sigma_0/\rho_f)^{1/2}] = 0.155$, Figure 20 plotted the midpoint displacement of steel substrate as a function of time for selected values of $d_{sr}/t_f$. Corresponding deformation processes of the sandwich-substrate were displayed in Figure 21 for $d_{sr}/t_f$=0 and $d_{sr}/t_f$=6. For the foregoing plotting, the sandwich had a fixed surface mass density of $M$ = 131.2 kg m$^{-2}$.

With the increase of $d_{sr}/t_f$, the distance between the front face of the sandwich and the geographic center of the charge (i.e., point $o$ on Figure 5) decreased, enabling more impulse transmitted to the sandwich according to eq. (3). Correspondingly, as shown in Figure 19, the residual deformation

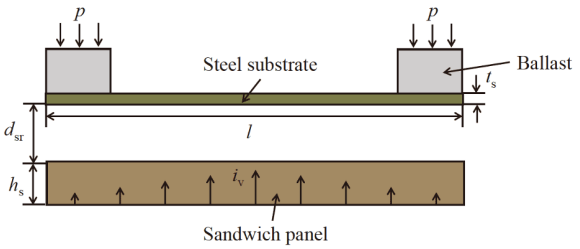


**Figure 18** (Color online) Schematic of sandwich-substrate combinative structure with a gap subjected to shallow-buried sand blast.

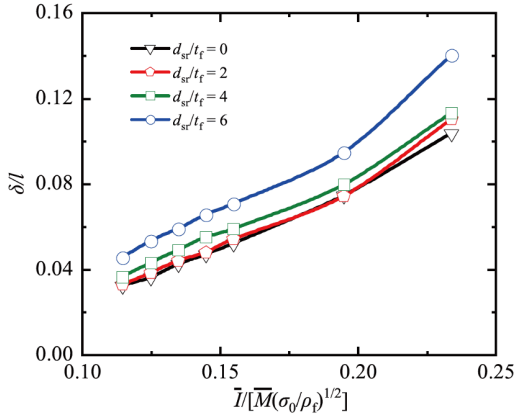


**Figure 19** (Color online) Normalized residual deformation of steel substrate plotted as a function of normalized impulse for selected gap thicknesses between substrate and sandwich panel.

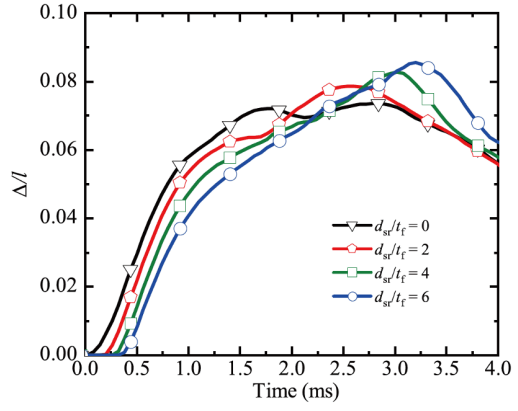


**Figure 20** (Color online) Midpoint displacement of steel substrate plotted as a function of time for selected gap thicknesses between substrate and sandwich panel, with $\bar{I}/[\overline{M}(\sigma_0/\rho_f)^{1/2}] = 0.155$.

of the steel substrate increased. The increase was initially linear, but gradually became nonlinear as the normalized impulse $\bar{I}/[\overline{M}(\sigma_0/\rho_f)^{1/2}]$ became sufficiently large. The results of Figure 20 revealed further that, as the value of $d_{sr}/t_f$ was increased, the initiation of the midpoint displacement of the substrate was delayed, accompanied with the increase of its peak and the time needed to reach this peak. This is because, with increasing $d_{sr}/t_f$, the deforming sandwich panel needs a certain time to contact with the substrate to transmit the blast impulse and energy, forcing the latter to move accordingly. The delayed movement of the substrate could also be seen from Figure 21(b).

### 5.2.2 *Connection conditions among sandwich panel, steel substrate and square frame*

Typically, for practical applications, the bottom plate of a vehicle was connected to its side wall while the protective structure was connected to the bottom plate. As shown in Figure 9, to facilitate the present FE simulations, the additional weight, steel plate and ballast placed on top of the test specimen (mimicking the weight of a vehicle; Figures 6 and 8), were simplified as a square steel frame of identical weight. However, the square frame was in direct contact with the steel substrate but the two were not connected together via, e.g., bolting or welding; similarly, the sandwich panel was not connected with the substrate. How the connecting conditions among the three main sub-structures (i.e., square frame, steel substrate and sandwich panel) affect the residual deformation of the substrate was quantified in this section. To this end, three different connecting conditions were considered. The first was considered already in previous sections and hence taken here as the reference, wherein the three sub-structures were in direct contact only. The second was identical to the first except that the square frame was perfectly connected with the steel substrate at the edges, with the connecting zone shown schematically in Figure 22(a). Built upon the second, the third condition assumed further that the steel substrate was perfectly connected with the back face of the sandwich panel at the edges, as shown in Figure 22(b). Numerically, for the second and third conditions, perfect connection was realized using "Tie" constraint.

Figure 23 displayed the predicted effects of connection condition on the residual deformation of steel substrate, with the surface mass density of the sandwich fixed at $\overline{M}$ = 131.2 kg m$^{-2}$. For the case of $\bar{I}/[\overline{M}(\sigma_0/\rho_f)^{1/2}]$=0.155, corresponding midpoint displacements of the steel substrate were plotted as functions of time in Figure 24, while the deformation process of the substrate-sandwich combination was presented in Figure 25. Relative to the reference case (i.e., the first type of connection condition), the results of Figures 23 and 24 revealed that both the residual deformation and midpoint displacement of the steel substrate decreased when perfect connection was present among the three sub-structures. This occurred because, upon connection, the heavy square frame restrained the steel substrate and the sandwich panel from sliding inwards, as shown in Figures 21 and 25. Compared with the second condition, the third condition led to further reduction in substrate residual deformation. These results demonstrated clearly the practical importance of connecting firmly the sandwich panel with the

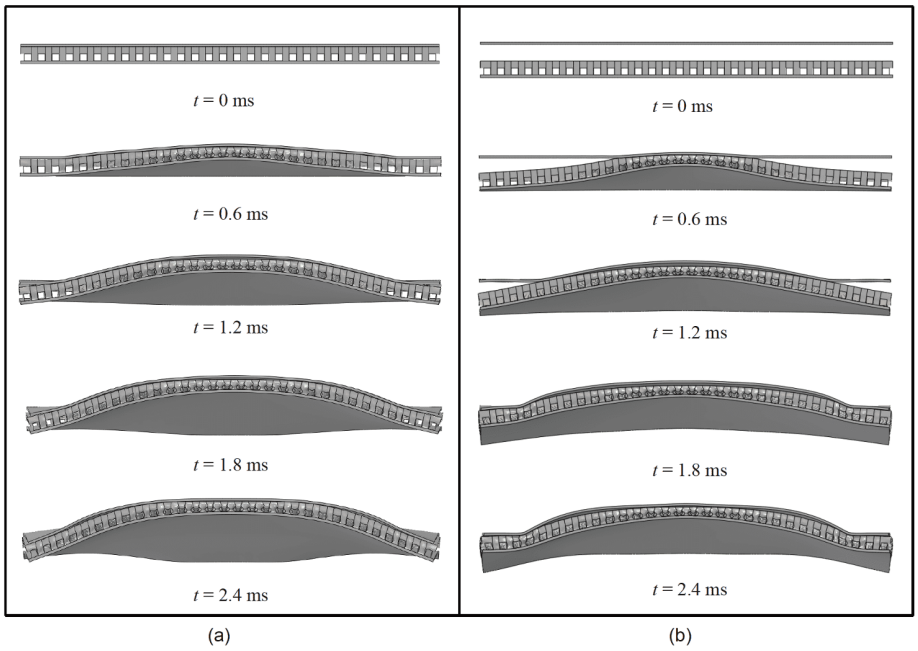


**Figure 21** Deformation process of sandwich-substrate combinatory structure under shallow-buried sand blast for (a) $d_{sr}/t_f$=0 and (b) $d_{sr}/t_f$=6, with $\bar{I}/[\overline{M}(\sigma_0/\rho_f)^{1/2}]=0.155$.

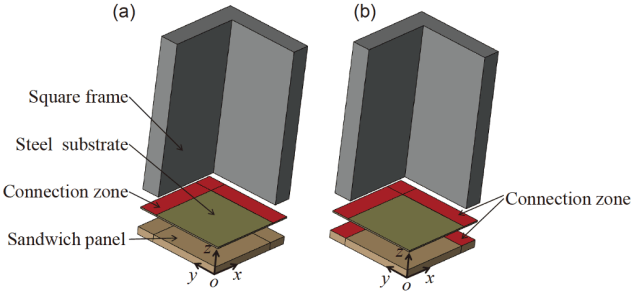


**Figure 22** (Color online) Connection zone between (a) square frame and substrate and (b) square frame, substrate and sandwich panel.

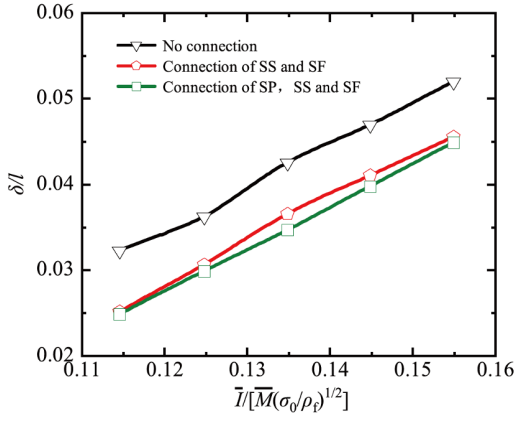


**Figure 23** (Color online) Effects of connection condition on residual deformation of steel substrate.

vehicle bottom for enhanced protection performance against blast.

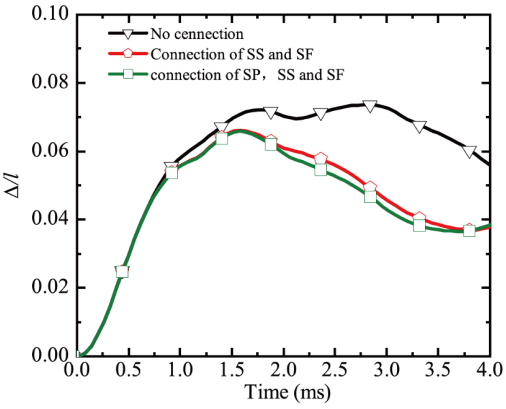


**Figure 24** (Color online) Midpoint displacement of steel substrate plotted as a function of time for the effects of connection condition, with $\bar{I}/[\overline{M}(\sigma_0/\rho_f)^{1/2}]=0.155$.

### 5.3 Comparison among competing sandwich core topologies

The dynamic performances of clamped sandwich beams having square honeycomb and corrugated cores were numerically compared with that of a monolithic beam with equal mass subjected to identical blast loading [20]. It was demonstrated that both types of sandwich beam exhibit superior blast resistance to the monolithic beam. As to a substrate-sandwich combinatory system, its dynamic behavior under blast loading remains elusive, irrespective of the type of core topology. This issue was addressed below using the numerical model of Figure 5, with three core types considered: square honeycomb, corrugated plate and 3D cellular

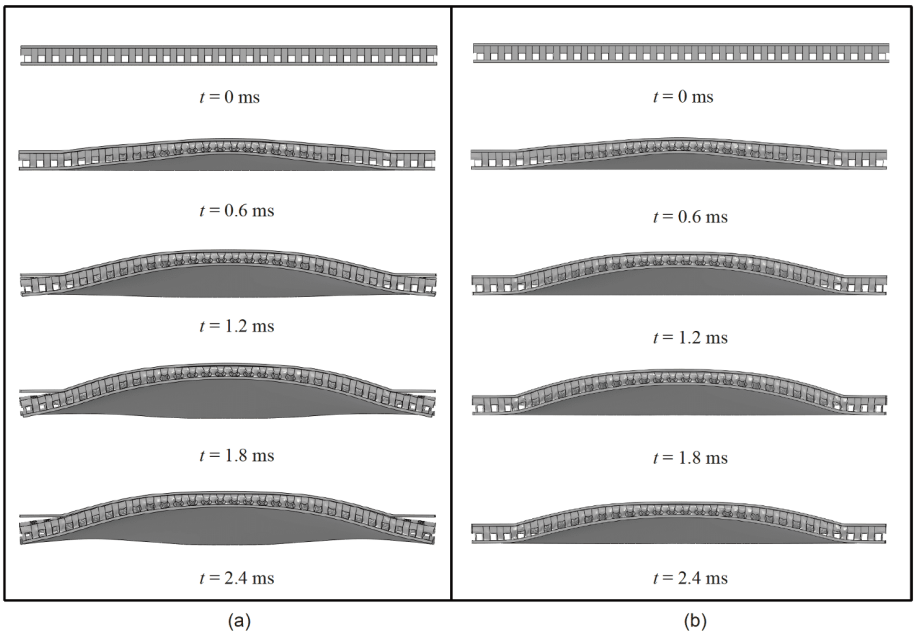


**Figure 25** Deformation process of substrate-sandwich combination ($\bar{I} / [\overline{M}(\sigma_0 / \rho_f)^{1/2}] = 0.155$). (a) Steel substrate and square frame connected; (b) square frame and sandwich panel both connected to steel substrate.

tubes. The square sandwich panel had fixed mass per unit area $\overline{M}$ = 131.2 kg m$^{-2}$, side length $l$=1500 mm, thickness of front face $t_f$=10 mm, thickness of back face $t_r$=1 mm, core height $h_c$=50 mm, and core relative density $\bar{\rho}$ = 0.115. We firstly assume that the front faces in the three different sandwich panels have identical mass, and so do their rear faces. Secondly, we vary the thickness of core plate to ensure that the three different cores have the same mass: as a result, the sandwich panels considered have identical mass. Thirdly, we assume these sandwich panels are of square shape, with identical side length $l$ (Figure 5). Consequently, in the current study, the three different sandwich panels have identical mass density per unit area. For the square honeycomb core, the cell width was 50 mm. For the corrugated core, the cell width was 200 mm, the inclination angle of corrugated wall was 45°, and the width of the connecting area between the front/back face and the core was 50 mm. For each sandwich-substrate system, the shallow-buried sand blast loading as detailed in Figure 6 was applied.

Figure 26 presented the influence of core morphology on residual deformation of the substrate, which revealed that the performance of the present 3D tube cellular core is almost the same as the square honeycomb, and both are superior to the corrugated core. This is attributed to the larger peak vertex displacement of the substrate achieved by the combinatory system with corrugated core relative to the other two core types, although its midpoint displacement is nearly the same as the other two, as illustrated in Figure 27. Note that the boundary condition of the sandwich-substrate system considered in the present study is significantly different from the fully-clamped boundary condition considered in ref. [20].

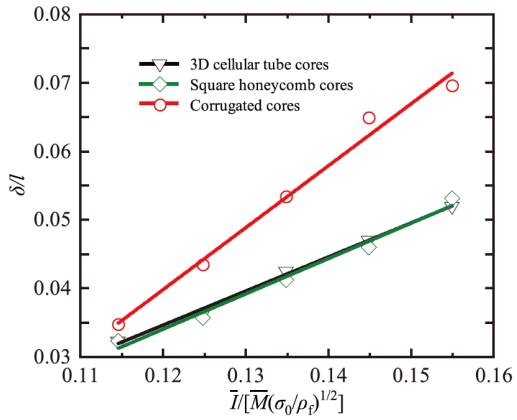


**Figure 26** (Color online) Effect of core topology on residual substrate deflection for sandwich-substrate combination subjected to shallow-buried sand blast, with $\bar{I} / [\overline{M}(\sigma_0 / \rho_f)^{1/2}] = 0.155$.

In addition, due to its relatively low out-of-plane (i.e., $z$-direction) compressive strength, the corrugated core is more severely compressed (particularly in the central region) compared to either the square honeycomb or the 3D tube cellular core, as demonstrated in Figure 28.

Aluminum hexagonal honeycombs with thin cell walls have been extensively used to construct ultralight sandwich structures, particularly for aerospace applications. Typically, for such honeycomb sandwich constructions, adhesive bonding is adopted to bond the cell walls as well as the core and the face sheets. For heavy-duty blast loadings like the one considered in the current study, however, sandwich structures cored with the classical aluminum hexagonal honeycombs having thin walls and adhesive bonding are not

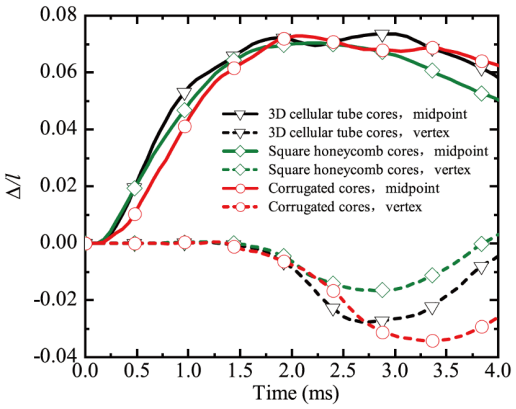


**Figure 27** (Color online) Effect of core topology on substrate midpoint and vertex displacements for sandwich-substrate combination subjected to shallow-buried sand blast, with $\bar{I}/[\overline{M}(\sigma_0/\rho_f)^{1/2}]=0.155$.

sufficiently strong and hence cannot meet the acute demand for energy absorption. As a result, sandwich structures with square honeycomb cores and metallurgical bonding via, say, laser welding or brazing, have been envisioned. To facilitate such metallurgical bonding between the face sheets and the square honeycomb core, the metal plates used to construct the core are typically much thicker than those of classical hexagonal honeycombs. Often, however, as thinner plates need to be employed to fabricate the square honeycomb core in order to minimize the weight of the sandwich, the plates need to be folded at their ends to form a platform to facilitate subsequent metallurgical bonding. The mass per unit area of the sandwich is therefore increased to a certain degree. In comparison, the proposed 3D tube cellular core can be bonded to the front and rear face sheets straightforwardly via laser welding or brazing. The results of Figure 26 reveal that the sandwich panel with 3D tube cellular core performs equally well as that with square honeycomb core of equal mass. Its potential for mitigating intensive blast loading in practical applications is therefore demonstrated. Nonetheless, it needs to be pointed out that, the sandwich panels considered for plotting the results of Figure 26 were not optimized, which will be the subject of forthcoming research.

### 5.4 Optimal design of 3D tube cellular core

The results above demonstrated the important role of sandwich core type played in residual deformation of the substrate. In particular, from Figures 13 and 14, the 3D tube cellular core was seen to contribute significantly to total energy absorption, especially the $z$-tubes. In this section, a preliminary optimal design of cross-sectional morphology was carried out for each tube type. To this end, the wall thickness, height and width of each tube were allowed to vary differently from the other tube types. Let the $x$-tubes have height $h_x$, width $w_x$ and wall thickness $t_x$. Let the $y$-tubes have height $h_y$, width $w_y$ and wall thickness $t_y$. Let the $z$-tubes have height $h_z$, width $w_z$ and wall thickness $t_z$. The distance between neighboring $x$-tubes as well as that between neighboring $y$-tubes were both assumed to be equal to $z$-tube width (i.e., $w_z$). Further, the square sandwich panel had fixed mass per unit area $\overline{M}=131.2\ \mathrm{kg\,m^{-2}}$, side length $l$= 1500 mm, thickness of front face $t_f$=10 mm, thickness of back face $t_r$=1 mm, core height $h_c$=50 mm.

For as-fabricated sandwich panels, $h_x=h_y=w_x=w_y=w_z=$ 25 mm, and $t_x=t_y=t_z$=1 mm. These were thence used as reference parameters for tube optimization. In addition, to minimize the calculation efforts, the following restrictions were employed.

(1) When optimizing the wall thickness (i.e., $t_x$, $t_y$ and $t_z$) for each tube type, the tube height and width were fixed at 25 mm while $t_x=t_y$ was assumed. Here, to ensure the mass of the tube core remain unchanged, both $t_x$ and $t_y$ were reduced (or increased) when $t_z$ was increased (or reduced).

(2) When optimizing the width and height of each tube type, it was assumed that $h_x=h_y$=25 mm, $w_x=w_y$, $w_x+w_z=$ 50 mm, and $t_x=t_y=t_z$ . To ensure the mass of the tube core remain unchanged, upon varying the tube width ($w_x$, $w_y$ or $w_z$), the tube wall thickness ($t_x$, $t_y$ and $t_z$) was varied accordingly.

Figure 29(a) and (c) displayed separately the variation of residual substrate deformation and plastic energy dissipation with the wall thickness of $z$-tubes for selected values of normalized impulse. Similar results were presented in Figure 29(b) and (d) when the width of $z$-tubes was systematically varied. Overall, when the $z$-tubes have relatively thin walls, increasing the wall thickness of the $z$-tubes (correspondingly, decreasing the wall thickness of $x$- and $y$-tubes due to equal mass constraint), led to significant reduction in substrate deformation and energy dissipation. The reduction however is less significant if the wall thickness of the $z$-tubes was sufficiently large, e.g., when $t_z/h_c$ exceeded 0.02. The influence of $z$-tube width $w_z$ exhibited similar variation trend, initially significant but gradually diminished as $w_z/h_c$ exceeded 0.4. Note that, in the current preliminary optimization study, the height of $z$-tubes was not varied as such variations

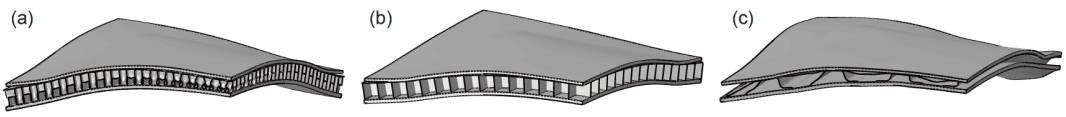


**Figure 28** Deformation mode of substrate-sandwich combination ($\bar{I}/[\overline{M}(\sigma_0/\rho_f)^{1/2}]=0.155$) with (a) 3D tube cellular core, (b) square honeycomb core and (c) corrugated core at $t$=4 ms.

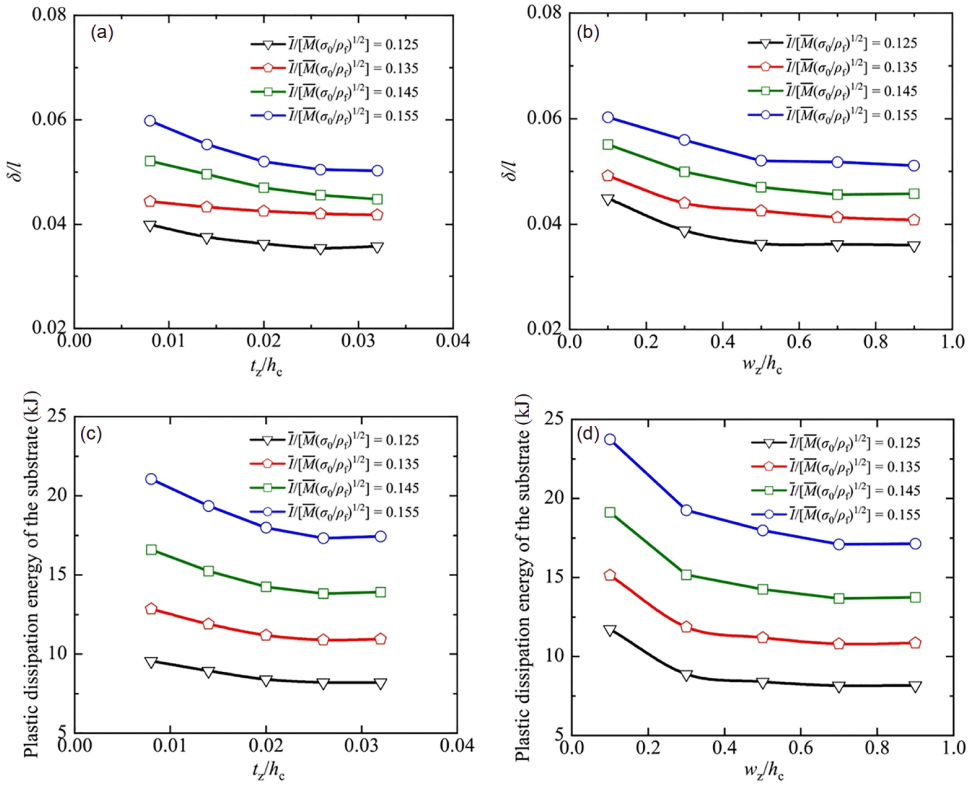


**Figure 29** (Color online) Residual deformation of steel substrate plotted as a function of (a) normalized thickness and (b) normalized width of *z*-tubes, and plastic dissipation energy of steel substrate plotted as a function of (c) normalized thickness and (d) normalized width of *z*-tubes.

would affect the distance between the front face and the explosives, thus affecting significantly the impulse transfer as indicated in eq. (3).

In summary, increasing the wall thickness or width of *z*-tubes could enhance significantly the blasting resistance of the present sandwich-substrate system, only if the wall thickness or width was relatively small compared to front face thickness.

## 6 Conclusions

The main motivation of this investigation was to use 3D tube cellular core to construct a novel type of sandwich panel and investigate its resistance response against blast loading caused by detonation of explosives shallow-buried in sand. To mimic the underbody of a vehicle, the proposed sandwich panel was used as an attachment to a substrate plate it aims to protect. Both experimental measurements and numerical simulations were carried out, with good agreement achieved. Physical mechanisms underlying the observed dynamic performance of the sandwich-substrate combination were explored, and the effects of key geometrical parameters and connection conditions of the protective system on such performance were quantified. For the sandwich-substrate combinatory structure subjected to shallow-buried sand blast, the dynamic performance of the 3D tube cellular core was compared to competing core topologies. It was demonstrated that, subjected to the constraint of equal mass, the proposed sandwich with 3D tube cellular core performed equally well as a honeycomb core sandwich, but was superior to a corrugated core sandwich. A preliminary optimal design carried out for each tube type revealed that increasing the wall thickness or width of *z*-tubes could enhance significantly the blasting resistance of the present sandwich-substrate system. In summary, the proposed sandwich structure with 3D tube cellular core is not only relatively easy to fabricate via, e.g., argon protected welding and laser welding, but also exhibits superior blast resistance at low weight, thus providing a valuable alternative for designing high-performance lightweight protection systems against intensive mine blasts and improvised explosive devices.

*This work was supported by the National Natural Science Foundation of China (Grant Nos. 11972185, 12002156 and 11902148), China Postdoctoral Science Foundation (Grant No. 2020M671473), State Key Laboratory of Smart Manufacturing for Special Vehicles and Transmission System (Grant No. GZ2019KF015), Natural Science Fund Project in Jiangsu Province (Grant Nos. BK20190392 and BK20190424), Open Fund of State Key Laboratory of Mechanics and Control of Mechanical Structures (Grant Nos. MCMS-E-0219K02 and MCMS-I-0219K01), and the Priority Academic Program Development of Jiangsu Higher Education Institutions (PAPD).*

**Supporting Information**

The supporting information is available online at tech.scichina.com and link.springer.com. The supporting materials are published as submitted, without typesetting or editing. The responsibility for scientific accuracy and content remains entirely with the authors.


1 Taylor L C, Skaggs R R, Gault W. Vertical impulse measurements of mines buried in saturated sand. Fragblast, 2005, 9: 19–28
2 Bocchieri R T, Kirkpatrick S W, Peterson B. Simulation-based design of vehicles exposed to blast threats for improved occupant survivability. WIT Trans Built Env, 2009, 1: 459–470
3 Børvik T, Olovsson L, Hanssen A G, et al. A discrete particle approach to simulate the combined effect of blast and sand impact loading of steel plates. J Mech Phys Solids, 2011, 59: 940–958
4 Pickering E G, Chung Kim Yuen S, Nurick G N, et al. The response of quadrangular plates to buried charges. Int J Impact Eng, 2012, 49: 103–114
5 Zhang X, Zhou Y, Wang X, et al. Modelling and analysis of the vehicle underbody and the occupants subjected to a shallow-buried-mine blast impulse. Proc Institution Mech Engineers Part D-J Automobile Eng, 2016, 231: 214–224
6 Dey S, Børvik T, Hopperstad O S, et al. The effect of target strength on the perforation of steel plates using three different projectile nose shapes. Int J Impact Eng, 2004, 30: 1005–1038
7 Uth T, Wadley H N G, Deshpande V S. The effect of inclination and stand-off on the dynamic response of beams impacted by slugs of a granular material. Int J Solids Struct, 2015, 56–57: 154–174
8 Johnson T E, Basudhar A. A metamodel-based shape optimization approach for shallow-buried blast-loaded flexible underbody targets. Int J Impact Eng, 2015, 75: 229–240
9 Goel A, Uth T, Wadley H N G, et al. Effect of surface properties on momentum transfer to targets impacted by high-velocity sand slugs. Int J Impact Eng, 2017, 103: 90–106
10 Kyner A, Deshpande V S, Wadley H N G. Impulse transfer during granular matter impact with inclined sliding surfaces. Int J Impact Eng, 2019, 130: 79–96
11 Grujicic M, Yavari R, Snipes J, et al. A combined finite-element/discrete-particle analysis of a side-vent-channel-based concept for improved blast-survivability of light tactical vehicles. Int J Struct Integr, 2016, 7: 106–141
12 Uth T, Deshpande V S. Response of clamped sandwich beams subjected to high-velocity impact by sand slugs. Int J Impact Eng, 2014, 69: 165–181
13 Geneviève T, Amal B, Robert D, et al. Numerical evaluation of an add-on vehicle protection system. In: Proceedings of the 9th European LS-DYNA Conference. Manchester, 2013
14 Rimoli J J, Talamini B, Wetzel J J, et al. Wet-sand impulse loading of metallic plates and corrugated core sandwich panels. Int J Impact Eng, 2011, 38: 837–848
15 Zhang P, Cheng Y, Liu J, et al. Experimental and numerical investigations on laser-welded corrugated-core sandwich panels subjected to air blast loading. Mar Struct, 2015, 40: 225–246
16 Dharmasena K P, Wadley H N G, Liu T, et al. The dynamic response of edge clamped plates loaded by spherically expanding sand shells. Int J Impact Eng, 2013, 62: 182–195
17 Liang Y, Spuskanyuk A V, Flores S E, et al. The response of metallic sandwich panels to water blast. J Appl Mech, 2007, 74: 81–99
18 Vaziri A, Hutchinson J W. Metal sandwich plates subject to intense air shocks. Int J Solids Struct, 2007, 44: 2021–2035
19 Kambouchev N, Noels L, Radovitzky R. Nonlinear compressibility effects in fluid-structure interaction and their implications on the air-blast loading of structures. J Appl Phys, 2006, 100: 063519
20 Xue Z, Hutchinson J W. A comparative study of impulse-resistant metal sandwich plates. Int J Impact Eng, 2004, 30: 1283–1305
21 Dharmasena K P, Wadley H N G, Xue Z, et al. Mechanical response of metallic honeycomb sandwich panel structures to high-intensity dynamic loading. Int J Impact Eng, 2008, 35: 1063–1074
22 Jing L, Wang Z, Zhao L. The dynamic response of sandwich panels with cellular metal cores to localized impulsive loading. Compos Part B-Eng, 2016, 94: 52–63
23 Wadley H N G, Børvik T, Olovsson L, et al. Deformation and fracture of impulsively loaded sandwich panels. J Mech Phys Solids, 2013, 61: 674–699
24 Yu B, Han B, Ni C Y, et al. Dynamic crushing of all-metallic corrugated panels filled with close-celled aluminum foams. J Appl Mech, 2015, 82: 47–55
25 Yu B, Han B, Su P B, et al. Graded square honeycomb as sandwich core for enhanced mechanical performance. Mater Des, 2016, 89: 642–652
26 Wang X, Yu R P, Zhang Q C, et al. Dynamic response of clamped sandwich beams with fluid-fillied corrugated cores. Int J Impact Eng, 2020, 139: 103533
27 Kyner A, Dharmasena K, Williams K, et al. Response of square honeycomb core sandwich panels to granular matter impact. Int J Impact Eng, 2018, 117: 13–31
28 Liu T, Fleck N A, Wadley H N G, et al. The impact of sand slugs against beams and plates: Coupled discrete particle/finite element simulations. J Mech Phys Solids, 2013, 61: 1798–1821
29 Li L, Han B, He S Y, et al. Shock loading simulation using density-graded metallic foam projectiles. Mater Des, 2019, 164: 107546
30 Zok F W, Waltner S A, Wei Z, et al. A protocol for characterizing the structural performance of metallic sandwich panels: Application to pyramidal truss cores. Int J Solids Struct, 2004, 41: 6249–6271
31 Holloman R L, Deshpande V, Wadley H N G. Impulse transfer during sand impact with a cellular structure. Int J Impact Eng, 2015, 82: 36–58
32 Holloman R, Deshpande V, Hanssen A, et al. Tubular aluminum cellular structures: Fabrication and mechanical response. J Mech Mater Struct, 2013, 8: 65–94
33 Holloman R, Kandan K, Deshpande V, et al. Dynamic compression of square tube cellular structures. J Mech Mater Struct, 2014, 9: 149–182
34 Tremblay J E. Impulse on blast deflectors from a landmine explosion. Technical Report. Quebec: Defence Research Establishment Valcartier, 1998. DREV-TM-9814
35 Clarke S D, Fay S D, Warren J A, et al. Predicting the role of geotechnical parameters on the output from shallow buried explosives. Int J Impact Eng, 2017, 102: 117–128
36 Yu R P, Wang X, Zhang Q C, et al. Effects of sand filling on the dynamic response of corrugated core sandwich beams under foam projectile impact. Compos Part B-Eng, 2020, 197: 108135
37 Jones N. Structural Impact. Cambridge: Cambridge University Press, 1989
38 Barsoum I, Faleskog J. Rupture mechanisms in combined tension and shear—Experiments. Int J Solids Struct, 2007, 44: 1768–1786
39 Nahshon K, Pontin M, Evans A, et al. Dynamic shear rupture of steel plates. J Mech Mater Struct, 2007, 2: 2049–2066